Pore Segmentation in Industrial Radiographic Images Using Adaptive Thresholding and Morphological Analysis

Dayana Palma **Ramírez**[1,*], Bárbara Dora Ross **Veitía**[1], Pablo Font **Ariosa**[2], Alejandro Espinel **Hernández**[1], Ramón Arias **Gilart**[1], Ángel Sánchez **Roca**[1], Hipólito Domingo Carvajal **Fals**[3]

[1] Centro Nacional de Electromagnetismo Aplicado. Universidad de Oriente;
[2] Defectoscopy and Welding Technical Services Company;
[3] Federal Technological University of Paraná;
* Correspondence: dayana.palma@uo.edu.cu

Abstract: In modern agriculture, the efficiency of agricultural machinery is crucial to achieve optimum performance. Inspection of weld quality becomes an essential component in assessing the integrity of machinery structures. This study presents an innovative approach by addressing pore segmentation in low-quality industrial radiographic images, using advanced image processing and adaptive segmentation techniques. The process aims to improve image quality for more accurate segmentation. It involves converting images to greyscale and applying Gaussian and Median filters. The methodology relies on adaptive thresholding and edge detection using Canny's algorithm, achieving highly accurate pore area measurements. Measurement errors are less than 0.1 mm², demonstrating the consistency and accuracy of the method. The model achieved precision, recall, and F1-Score metrics of 97.52%, 98.33%, and 97.92%, respectively. These values underscore the model's applicability in the task of segmenting radiographic images, showcasing its ability to achieve accurate identification of regions of interest and provide reliable measurements. Although further research is needed to improve contrast and illumination and address potential sources of error, these refinements have the potential to enhance an already reliable and accurate method with a wide reach in industry. The method presented not only provides a solution for pore detection in radiographic images but also proves to be a valuable asset for industrial radiography applications, encompassing quality control, defect analysis, and demonstrating potential applications in modern agriculture and production engineering.

Keywords: radiographic image segmentation; adaptive thresholding; pore detection; industrial radiography; morphological analysis.

1. Introduction

Welding is a critical aspect of manufacturing and maintaining agricultural equipment. It directly impacts the efficiency, durability, and safety of equipment such as tractors, harvesters, and seeders. These machines are frequently exposed to external factors like wind, harsh weather conditions, and dirt accumulation in their operating environment (Melibaev et al., 2022). Inspection of weld quality has become vital in ensuring reliable performance of agricultural machinery. The integrity of welds affects not only the structural robustness of equipment but also operator safety and operational efficiency. Thorough assessments of joints and critical points of structures are necessary for inspecting weld quality (Szusta et al., 2023).

The quality of welds is crucial in numerous industries, including construction, aerospace, automotive, and agriculture (BD, 2020; Hernández et al., 2020; McPheron & Stwalley, 2022; Pérez de la Parte et al., 2022; Wang et al., 2021). The presence of defects in welds, especially

pores, can have serious consequences ranging from loss of structural integrity to threatening the safety and performance of products and structures (Yahaghi et al., 2021). Pores, which are small cavities or holes in welds, can be filled with gases resulting from metal contamination or metal melting, and their negative impact is undeniable. They weaken the weld joint, reduce its mechanical strength, and facilitate corrosion (Li et al., 2022). In addition, pores can serve as starting points for the formation of cracks and fractures, potentially leading to catastrophic failures in critical components (Jonsson et al., 2016).

Efficient pore segmentation in industrial radiographic imaging is a key technological tool at the intersection between material science and agricultural challenges. Advanced image processing techniques are used for pore segmentation, making it an indispensable instrument that contributes to strategic planning and the implementation of more efficient and sustainable agricultural practices. Accurately identifying and measuring pores within agricultural equipment structures is crucial in assessing the quality of welded joints and operational efficiency (Açar et al., 2023; Haievskyi et al., 2020; Kappaun et al., 2021; Wells & Miller, 2022).

In this context, industrial radiography emerges as a valuable tool for detecting pore defects in welds and, in general, as a nondestructive method to evaluate the quality of welded joints (Dwivedi et al., 2018; Golodov & Maltseva, 2022; Patil et al., 2021; Tyystjärvi et al., 2022; Wang & Gao, 2021; Wang & Yu, 2023; Zhang et al., 2023). Industrial radiography detects non-visible defects in materials using shortwave X-rays, gamma rays, and neutrons, revealing pores or discontinuities (Rafiei et al., 2023). This technique offers several advantages, such as the ability to inspect welds of varying thicknesses, identify subsurface defects, and evaluate welds in hard-to-reach areas. In addition, industrial radiography is fast and efficient, (Eckel et al., 2020; Liu et al., 2022; Wang et al., 2022) resulting in an effective and time-saving nondestructive inspection.

Image processing is integrated essentially into this inspection technique (Ríos et al., 2022). It provides greater accuracy in the detection and characterization of pore defects in welds, even those of microscopic dimensions that may escape conventional visual observation. It allows pores to be segmented and classified efficiently, providing detailed information about their size, shape, and location. Ultimately, image processing contributes to an accurate assessment of weld quality, which is critical in industries where integrity and safety are priorities (Zhan et al., 2018).

Several authors have focused their studies on digital image processing techniques to segment weld defects in radiographic images. In the research of Liu et al. (Liu et al., 2022), the authors propose a new approach based on an improved Chan-Vese model to detect weld defects in X-ray images. This improved model consists of three stages: in the first, the region of interest is detected; in the second, the Fuzzy C-Mean (FCM) algorithm is used to choose a group as the initial contour; and in the third, the Chan-Vese model is applied with the selected initial contour to segment the images and obtain the defect boundaries.

On the other hand, Radi et al. (Radi et al., 2022) use convolutional neural networks (CNN) to segment horizontal defects and separate background and vertical defects. And in the research of Gong et al. (Gong et al., 2022) relies on transfer learning to use Faster R-CNN for localization and detection of small defects.

Threshold segmentation, a classic technique in image processing, stands out for its efficiency in terms of computational resource usage and speed of execution. Because of these advantages, it has become a frequent choice in industrial X-ray inspection applications. The wide applications of common thresholding methods, such as adaptive thresholding (León Ovelar et al., 2021), Otsu thresholding (Niño et al., 2021), and others have been investigated by several researchers.

Duan et al. (Duan et al., 2019) use adaptive thresholding to extract defects that are subsequently classified using the adaptive cascade boosting algorithm (AdaBoost). On the other hand, Zhang et al. (Zhang et al., 2018) combine the adaptive thresholding segmentation algorithm and

mathematical morphology reconstruction, and the results obtained by these authors validate the use of these techniques in radiographic image segmentation.

Aslam et al. (Aslam et al., 2019), combine the Cuckoo Optimization Algorithm (COA) with adaptive thresholding to solve the problem of detection and estimation of surface defects on metallic surfaces. The proposed method was able to adapt the dynamic step size, adaptively changing with the search to improve the convergence rate and local search capability.

Truong et al. (Truong & Kim, 2018) present an automatic thresholding technique that represents an improvement over Otsu's approach by incorporating an entropy-based weighting scheme. This methodology can identify areas with defects of reduced dimensions about the total surface area of the product. Other authors such as Liu et al. (Liu & Yang, 2017) use Otsu's thresholding method to identify the characteristics of holes inside the concrete surface.

In a similar research Li et al. (Li et al., 2023) designed an adaptive threshold segmentation module that performs the threshold segmentation of the SU-Net network model, which verifies the feasibility of this method. The use of adaptive thresholding is chosen by the authors for its ability to process images with uneven illumination as is the case in the research of Contreras et al. (Contreras et al., 2022). This type of classical approach allows to perform image segmentation by separating the defect from the background and is very useful in processing noisy images.

Throughout the literature, several authors use adaptive threshold segmentation in various applications using radiographic images. However, it should be noted that this technique tends not to be frequently applied in low-quality images, such as those presented by CENEX (Defectoscopy and Welding Technical Services Company) where other approaches are often preferred. In addition, it is important to mention that few studies combine adaptive thresholding with mathematical morphological analysis for accurate calculation of defect area. Therefore, in this research, these techniques are used in image processing with uneven illumination, noise, and low contrast.

2. Materials and Methods

The set of radiographic images used in the welding defect segmentation task is composed of radiographs that are part of the historical archive of CENEX in Cuba. 50 samples were selected from a set of images that have been collected over more than 10 years, which means that the digitization conditions have not been constant in all of them. The samples are of dimensions 300x300 pixels and relate to welds that exhibited pore defects, evenly distributed between individual pore defects and pore clusters.

To carry out the segmentation experiments, we took advantage of a Google Colab instance equipped with an Nvidia Tesla T4 GPU. This configuration was essential to accelerate the processing of fundamental libraries in the field of image processing, such as OpenCV, NumPy, and scikit-image. The choice of this platform was based on its accessibility, ease of use, and availability of computational resources, which enabled the efficient execution of experiments without incurring additional costs.

Image processing involves several stages, as detailed in Figure 1. In the first stage, an image in RGB format, containing multiple color channels, was used as input to the process. To simplify processing and reduce data complexity, the original image was transformed to grayscale. This transformation involved converting the image from three color channels (red, green, and blue) to a single channel representing the luminous intensity in each pixel.
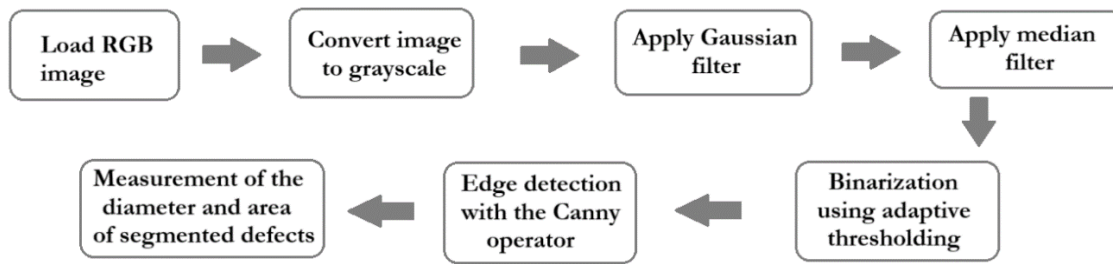
Figure 1. Algorithm for radiographic image processing, edge detection, and defect characterization.

Next, several filters were applied to improve the image quality and prepare it for pore segmentation. A Gaussian filter was used to smooth the image and reduce noise, followed by a median filter to further remove any unwanted interference.

Next, the pore segmentation stage was performed using an adaptive thresholding technique. This technique identified areas of interest in the image where pores were suspected to be located. Subsequently, the Canny edge detector was applied to highlight the contours of the pores and define their boundaries more clearly.

Finally, a morphological analysis of the segmented image was performed to measure the area of the identified pores. To perform the calibration, a known length must first be accurately measured in the original image, which can be achieved by using an object with known real dimensions or a reference in the image that is measurable in the real world, such as a ruler. For this purpose, a conversion factor relating pixels in the image to units of millimeters was used, allowing accurate measurements of pores in terms of size and distribution to be obtained. To find this conversion factor, the image quality indicator (IQI) measurements used at CENEX for the analysis of these images were used.

IQIs are objects that are placed next to the object to be radiographed and help to evaluate the quality of the radiographic image. In the context of DIN standards, a "DIN Wire Type IQI" refers to an image quality indicator that uses reference wires with specific sizes and characteristics to verify the quality of radiographic images. For this research, images presenting a 6 FE DIN IQI were analyzed. The dimensions of this indicator are illustrated in Table 1 according to DIN EN ISO 19232-1.

Table 1. IQI 6 FE size and wire identification numbers.

Wire Diameter	Wire Identity
0.0393" (1.00 MM)	6
0.0315" (0.80 MM)	7
0.0248" (0.63 MM)	8
0.0196" (0.50 MM)	9
0.0157" (0.40 MM)	10
0.0126" (0.32 MM)	11
0.0098" (0.25 MM)	12

To perform the calibration, the dimensions of each wire were taken on 10 sample images to obtain robust and reliable measurements. By working with multiple images, it is possible to capture the variability that may be present due to factors such as camera position and focus, as well as possible fluctuations in lighting conditions. This strategy of acquiring a larger data set reduces the influence of potential outliers or random errors in a single measurement. This broad

image-processing scheme allowed detailed information on the morphology of the pores in the radiographs to be obtained, which facilitated the analysis and characterization of these components in the study.

2.1 Image processing

The choice to change the original X-ray images, originally in RGB format, to a grayscale representation was based on the need to perform a quantitative analysis of the porosity. This transformation was performed using the OpenCV function cv2.cvtColor, which assigned each pixel a unique value reflecting its intensity in shades of gray. This modification became essential to eliminate unnecessary color information and simplify the analysis process by focusing exclusively on light intensity. This simplified approach proved beneficial for the subsequent stages of analysis.

The need to apply filters to images is based on the presence of noise, specifically Gaussian and salt and pepper noise. Noise in images can be problematic, as it introduces unwanted variations in pixel intensity, which negatively affects image quality and can make it difficult to detect and segment objects of interest. In the case of Gaussian noise, this type of noise introduces random fluctuations in pixel intensity values, often resulting in an image with a "fuzzy" or finely textured grainy appearance.

To counteract this effect and improve image contrast, a Gaussian filter was applied. This filter was applied after converting the original X-ray images from RGB to grayscale format, for quantitative porosity analysis. The kernel size of the filter was set to (11, 11), which indicated that a window of 11x11 pixels was used for smoothing. The standard deviation in the horizontal direction was left at 0, allowing OpenCV to automatically calculate its value based on the kernel size.

The Gaussian filter played a crucial role in counteracting the adverse effects of Gaussian noise in the images (Kumar & Sodhi, 2020). By removing high-frequency fluctuations, this filter was able to smooth the image, thus generating a more uniform and easier-to-process representation. The application of this smoothing technique provided a significant improvement in the overall image contrast, which played an essential role in the pre-preparation of the images before carrying out additional stages of analysis and segmentation of the defects in the welds.

On the other hand, salt and pepper noise is a type of noise that causes extremely dark pixels (pepper) and extremely bright pixels (salt) to appear in the image. This type of noise can be very disruptive and make it difficult to detect important objects and features (Liang et al., 2021). To mitigate this effect, a median filter was also applied, which in this case was responsible for removing or reducing the salt and pepper pixels, thus restoring image coherence. The median filter was set to a window size of 45x45 pixels. This choice was the result of previous experimentation and resulted in a filtered image that preserved relevant details while removing unwanted noise. In the research of Hu, A. et al. (Hu et al., 2022), the use of this filter in radiographic images is validated.

The combination of these two filtering strategies helped to improve the quality of the images, which facilitated the segmentation and subsequent analysis of the weld defects. This pre-processing is essential to ensure that the objects of interest are clearly defined and accurately measurable in the image. It also helps to eliminate noise and illumination variations that can affect the detection and measurement of pores and cracks in welds.

After applying the median filter, binarization of the images was performed. Binarization is a specific process that involves the conversion of a greyscale or color image to a binary image. In a binary image, each pixel is assigned to one of two possible values, usually 0 (black) or 255

(white), where 0 represents the background or unwanted regions, and 255 represents objects of interest, such as pores, edges or other elements to be highlighted. Binarization is based on a threshold that determines when a pixel is assigned to one class or another and can be global (the same threshold for the whole image) or local (different thresholds for different regions of the image) (Choi & Ha, 2023). The basic formula for binarization can be expressed as follows (1):

$$T(x, y) = f\left(I_{neighborhood}(x, y)\right) \tag{1}$$

where $T(x, y)$ is the threshold calculated for the pixel at position (x, y), f is a function that calculates the local threshold as a function of the characteristics of the neighbourhood of the pixel and $I_{neighborhood}(x, y)$ represents the characteristics or statistics of the neighborhood around the pixel (x, y), which may include mean, median, standard deviation, etc., depending on the specific method.

The algorithm for applying thresholding is as follows (2):

$$Binarized\ Pixel = (Original\ Pixel > Threshold)\ ?\ White\ Value : Black\ Value) \tag{2}$$

where Binarized pixel is the pixel value in the binary image (usually 0 for black and 255 for white), Original pixel is the value of the pixel in the greyscale image, Threshold is the threshold value that determines whether a pixel is assigned to the black or white value, White value is the value assigned to the pixel if the condition (Original pixel > Threshold) is true (usually 255 or white), and Black value is the value assigned to the pixel if the condition (Original Pixel > Threshold) is false (usually 0 or black).

The filtered images were binarized using the adaptive thresholding method. This process separates the image into regions of white (pores) and black (backgrounds) pixels. Adaptive thresholding is used to divide an image into smaller regions and apply different thresholds to each of these regions. This is useful when the image illumination varies significantly in different parts of the image. The choice of threshold is critical and can be a fixed value (global threshold) or adaptively calculated for different regions of the image (adaptive threshold). The threshold value may vary depending on the application and the nature of the image.

In adaptive thresholding, the threshold is calculated based on local image properties, such as the average or standard deviation in a neighborhood around each pixel, which allows for more robust binarization in images with irregular illumination or contrast variations. The segmentation in this work was performed using the cv2.ADAPTIVE_THRESH_MEAN_C method in OpenCV, known as mean-based adaptive thresholding (3). In this research, a block size of 101x101 pixels was used to calculate the local thresholds.

$$T(x, y) = mean\left(I_{neighborhood}(x, y)\right) - C \tag{3}$$

where C is a constant, which is not constrained to a specific range and can vary depending on the context of the application and the characteristics of the processed images.

The algorithm followed in using this method was as follows:

1. The grayscale image is divided into small regions or blocks of size 101x101. In each of these blocks, a local threshold is calculated.

2. To calculate the local threshold in each block, the average of the pixel values within that block is taken and a constant (C) is subtracted.

3. After calculating the local thresholds for all blocks in the image, these thresholds are then applied to the entire image. Each pixel is subjected to a comparison with the corresponding threshold in its block, resulting in its binarization to white (255) if its value exceeds the local threshold or to black (0) if its value is less than or equal to the local threshold. This process is repeated for each region of the image, where a local threshold is calculated based on the intensity statistics of that specific region. Pixels exhibiting intensities below this local threshold are assigned to black, while those above the threshold are assigned to white. If a region containing a defect exhibits an average intensity that is lower than its local threshold, pixels representing the defect are marked as black.

This adaptive thresholding approach is useful when the illumination is not uniform throughout the image or when there are significant variations in contrast in different parts of the image as presented in these CENEX images. Instead of using a global threshold, it adapts locally to image features in small regions, which can improve segmentation accuracy.

Once the images were segmented, the Canny operator was applied to detect the edges and contours of the objects of interest in the binarized image. This helps to clearly define the shape and location of the pores. Edge detection with thresholds of 50 and 150 was applied to highlight relevant details in the images.

The mathematical formula for the Canny operator can be expressed in general terms as follows:

1. Gradient Detection: First, the gradients of the image are calculated to find the areas of rapid change in pixel intensity. This is done by applying convolution operators such as the Sobel operator in the horizontal and vertical directions. These gradients are calculated as follows (4):

$$G_x = I * K_x$$
$$G_y = I * K_y$$

(4)

where G_x and G_y are the gradient images in the horizontal and vertical directions, respectively, I is the original image, K_x and K_y are the kernels of the Sobel operator or any other gradient operator used.

2. Gradient Magnitude and Direction: Next, the magnitude of the gradient at each pixel is calculated using the gradient images G_x and G_y. The magnitude of the gradient is calculated as (5):

$$Magnitude = \sqrt{G^2{}_x + G^2{}_y}$$

(5)

The direction of the gradient, which represents the direction of maximum change in intensity, is also calculated and is obtained using the arctangent function (6):

$$Direction = atan2(G_x, G_y)$$

(6)

3. Non-maximum suppression: To reduce edges to a single line of pixels wide, non-maximum suppression is applied. This involves traversing the image and, for each pixel, checking whether its gradient magnitude is a maximum in the direction of its gradient. If it is, it is retained as an edge pixel; otherwise, it is suppressed.

4. Hysteresis thresholding: Finally, hysteresis thresholding is applied to detect end edges. Two thresholds are used, one high and one low. Pixels with gradient magnitude above the high threshold are considered strong edge pixels, and pixels below the low threshold are discarded. Pixels whose gradient magnitude lies between these two thresholds are considered weak edge pixels. However, if a weak edge pixel is connected to a strong edge pixel, it is considered part of the final edge.

2.2 Mathematical morphological operations

After edge detection, mathematical morphological operations, such as dilation with a 5x5 pixel kernel, are applied to further improve object detection. These operations are used to connect nearby regions of pixels and remove small unwanted details, which facilitates subsequent measurements. After carrying out these operations, morphological analysis is performed to calculate the diameter and area of the detected contours, known as morphological analysis based on mathematical morphology. This process allows measuring and characterizing the properties of the objects and regions present in the image, in this case focusing on the contours identified during edge detection. In addition, a record is kept of the number of contours identified in the images to determine the number of pores in the samples.

To measure the characteristics of each contour, the diameter of the object in pixels is calculated by obtaining the minimum circle surrounding it, using the function cv2.minEnclosingCircle. Subsequently, a unit conversion is performed to express the pore area in square millimeters (mm²), following the algorithm described in Figure 2.
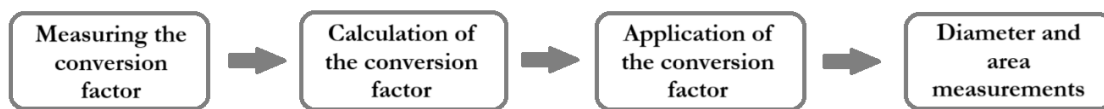

Figure 2. Algorithm to find and apply the conversion factor to measure the area of defects found in radiographic images.

The standard deviation was calculated to measure the dispersion of the data about the mean value, and the error in the measurements was calculated to assess their precision and understand the associated uncertainty. These analyses are crucial to determine the reliability of the measurements in the context of the sample images.

Once the length in pixels has been measured and its actual length in millimeters is known, the conversion factor is calculated by dividing the actual length by the length in pixels. This conversion factor indicates how many pixels correspond to one millimeter in the image. In the sample images, the resulting conversion factor was 0.00943 pixels per millimeter.

The conversion factor previously calculated, is then applied to the measurements made on the images. This allows the dimensions of objects and features to be accurately converted from pixels to millimeters. Therefore, this factor ensures that the dimensions of the objects captured in the image are correctly related to the dimensions of the physical world, providing accurate and applicable measurements in the evaluation of the objects of interest in the image.

2.3 Evaluation metrics

The performance of the algorithm was evaluated by comparing metric results, calculated using the Python Scikit-learn package (Batallas et al., 2020). The quantitative assessment of the algorithm's performance includes precision, recall, and F1 Score, analyzing its capability for accurate segmentations. These metrics are defined using the abbreviations TP (true positives), TN (true negatives), FP (false positives), and FN (false negatives).

Precision: The proportion of true positives (TP) among all cases classified as positive by the model (TP + FP). It is useful when false positives are to be minimized (7).

$$Precision = \frac{TP}{(TP + FP)} \tag{7}$$

Recall: It is the proportion of true positives (TP) among all positive cases present in the test data (TP + FN). Sensitivity is used when it is crucial to identify all positive cases, even if this implies having some false positives (8).

$$Recall = \frac{TP}{(TP + FN)} \tag{8}$$

F1-Score: It is a metric that combines precision and sensitivity into a single measure that provides a balance between the two. It is calculated as the harmonic mean of accuracy and sensitivity, and is useful when seeking a balance between accurately identifying positive cases and minimizing false positives (9).

$$F1 - Score = \frac{2(Precision * Recall)}{(Precision + Recall)} \tag{9}$$

These metrics provide a quantitative assessment of the model's performance by analyzing its ability to perform accurate segmentations.

3. Results and Discussion

The set of images presents notable challenges, such as reduced contrast, non-uniform gray level distribution, the presence of noise, and variations in illumination. The RGB images are shown in Figure 3(a).
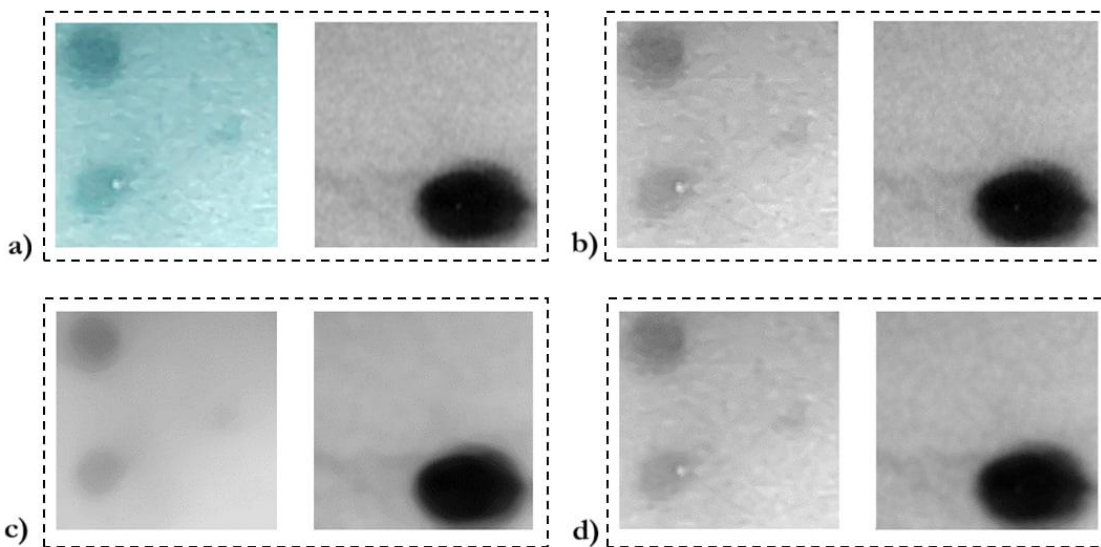

Figure 3. Original images **(a)**, images converted to grayscale **(b)**, Gaussian filtered images **(c)**, Median-filtered images **(d)**.

The result of applying greyscale conversion of these images after applying the OpenCV cv2.cvtColor function, is illustrated in Figure 3(b). In Figure 3(c) and Figure 3(d) the same images are shown after applying the Gaussian and Median filter respectively.

The filtered images were binarized using the adaptive thresholding method. The choice of the optimal value of the constant (C) in the segmentation process is crucial to obtaining accurate and meaningful results. The main goal of segmentation is to accurately distinguish areas of interest from the background in an image.

When analyzing Figures 4(a) and 4(b), with lower C values (2 and 4), it is observed that the algorithm does not achieve an effective separation, confusing the background with the objects of interest. This indicates that these C values are not suitable for this application.
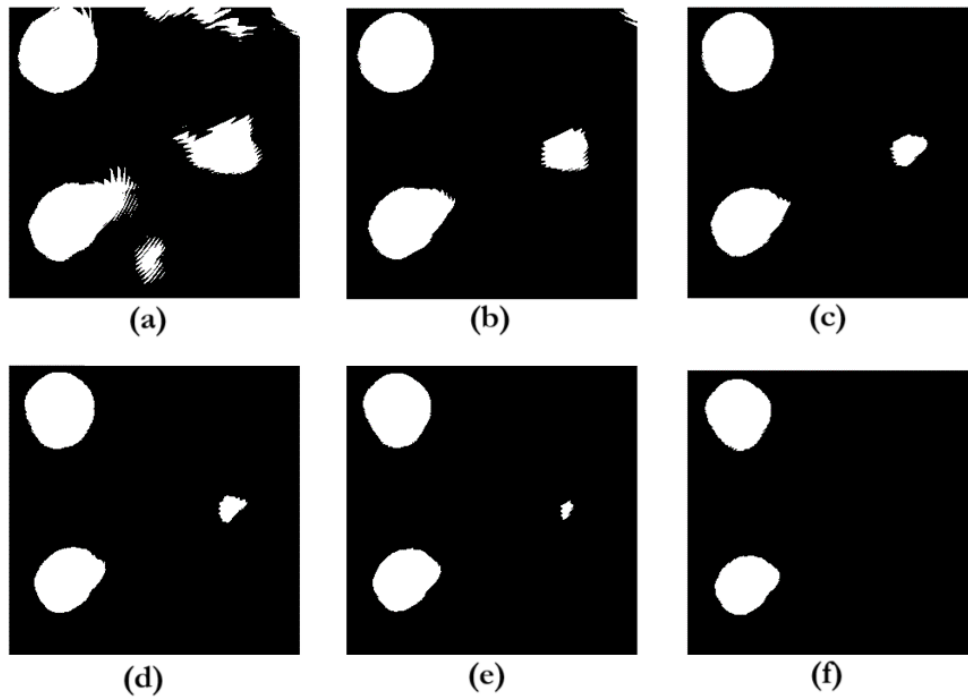

Figure 4. Segmented images using adaptive thresholding with different C values: **(a)** C = 2; **(b)** C = 4; **(c)** C = 6; **(d)** C = 8; **(e)** C = 10; **(f)** C = 12.

As the value of C increases, there is an improvement in the resolution of details in the segmentation, as is evident in Figures 4(c) and 4(d) with C = 6 and C = 8, respectively. With C = 8, objects are better distinguished, and a clearer segmentation is achieved. This is essential when looking for sharp contours and adequate separation between the objects of interest and the background. In Figures 4(e) and 4(f), with higher C values (C = 10 and C = 12), a loss of detail and a tendency to over-segmentation is observed. This means that the algorithm is dividing the image into smaller regions than necessary, which could lead to the loss of important information and a less accurate interpretation of the image. The choice of C = 8 seems to strike the right balance between detail resolution capability and minimizing over-segmentation. While there may still be areas that are not perfectly segmented, this value of C achieves generally satisfactory results, as evidenced in Figure 4(d).

The value C = 8 is considered the optimal constant for segmentation in this particular context due to its ability to achieve an effective balance between discrimination, detail resolution, and prevention of over-segmentation. This choice was based on the evaluation of multiple factors and effectively fits the needs of this particular study. It is important to note that the choice of this value may vary depending on the application and the specific characteristics of the images, but in this context, C = 8 offers a balanced and adequate performance. The result of applying the value of C=8 in the image binarization process is shown in Figure 5 in two sample images.
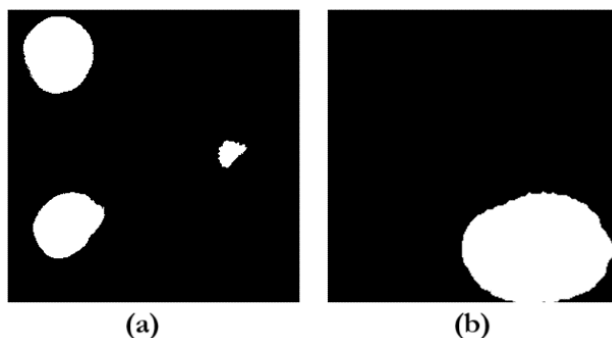
Figure 5. Segmented images using adaptive thresholding: **(a)** group of pores; **(b)** pore.

Figure 6 illustrates the outcome of applying the Canny algorithm to detect pore contours in the binarized images. This process highlighted the edges of the pores, enabling enhanced visualization and analysis of the features of interest.
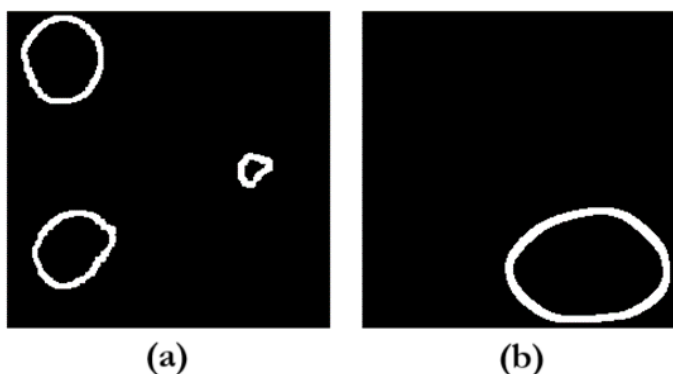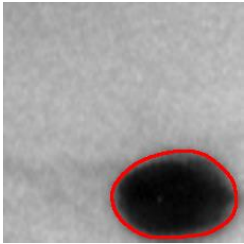

Figure 6. Representation of defect contours: **(a)** group of pores; **(b)** pore.

The result of the application of the conversion factor to the sample images is illustrated in Table 2, where a comparison of the results obtained by CENEX specialists and the proposed algorithm for the analyzed images is made. The areas marked in red represent the contours detected by the algorithm proposed in this study in three sample images.

Table 2. Comparison of the dimensions of the defect areas calculated by the certified experts and the proposed algorithm.

Image	Number of contours	Defect area calculated by expert	Defect area calculated in this research	Area Difference	Percentage Difference
	1	1.00 mm2	0.9698 mm2	0.0302 mm2	3.02%

Image	Number of contours	Defect area calculated by expert	Defect area calculated in this research	Area Difference	Percentage Difference
	1	0.60 mm2	0.4957 mm2	0.1043 mm2	10.43%
	1	0.55 mm2	0.5040 mm2	0.046 mm2	4.6%
	1	0.20 mm2	0.1006 mm2	0.0994 mm2	9.94%
	1	0.40 mm2	0.3297 mm2	0.0703 mm2	7.03%
	2	-	0.1230 mm2	-	-

Table 2 presents a comparison between the defect areas calculated by an expert and the defect areas calculated in the course of this research on two samples. These measurements are essential for the evaluation of the quality and integrity of X-ray images, especially in applications where accuracy is essencial, such as the detection of defects in materials.

A key observation from Table 2 is that the defect areas calculated in this research are notoriously similar to those provided by the expert as the percentage differences between the areas calculated by this algorithm and that reported by the experts range from 3.02% to 10.43%.

Furthermore, it can be noted that the errors in the measurements in no case exceed 0.1 mm². This consistency indicates that the measurement approach used in the research is consistent and not significantly affected by external factors or variability in the images.

However, it is important to note that this algorithm detects a defect that was not identified by the certified experts. This difference could be due to several reasons, such as possible variations in the measurement technique, interpretation of the defect boundaries, or the quality of the images, which could have hindered an accurate measurement by the experts. The interpretation of this result is that it is a false positive.   The comparison between the defect areas calculated by the algorithm and those provided by CENEX shows consistency in the analysis method used. However, any systematic trends leading to significant differences should be investigated and addressed to further improve the accuracy of the method and ensure quality in inspection and quality control applications. The algorithm detected a total of three false positives and two false negatives. The results of the evaluation metrics are detailed in Table 3.

Table 3. Values of the metrics obtained by the proposed algorithm in the segmentation of the images.

Metrics	Values
Precision (7)	97.52%
Recall (8)	98.33%
F1-Score (9)	97.92%

The results in Table 3 indicate a solid performance on the segmentation task, revealing an accuracy of 97.52%, a recall of 98.33%, and an F1-Score of 97.92%. The accuracy of 97.52% suggests that most of the pixels classified as part of the segmentation are, in fact, part of the region of interest, reflecting a low false positive rate. On the other hand, the recall of 98.33% indicates that the model is capturing the vast majority of the relevant pixels in the segmentation, demonstrating an outstanding ability to correctly identify the region of interest. The F1-Score, which combines precision and recall, reaches a solid 97.92%, underlining an effective balance between both metrics and highlighting the robustness of the model in the segmentation task.

Table 4 presents the average values of pore areas, measured in the 50 images by certified experts from CENEX. These results are compared with the areas calculated by the proposed algorithm.

Table 4. Average values of pore areas calculated by certified experts and the proposed algorithm in the 50 sample images.

	Average Value
Defect area calculated by expert	1.78 mm²
Defect area calculated in this research	1.7968 mm²
Area Difference	0.0496 mm²
Percentage Difference	4.96%

It is relevant to note that the area calculated by the algorithm shows a smaller size compared to that reported by the experts, which highlights the accuracy of the measurement performed by the algorithm. This difference could be related to the algorithm's ability to more accurately detect defect boundaries, resulting in slightly smaller defect areas compared to the experts measurements. This feature is of great importance as it demonstrates the algorithm's ability to

provide more accurate and consistent measurements in defect detection, which can be critical in inspection and quality control applications.

The algorithm used in this study demonstrates a remarkable advantage in detecting defects that sometimes go unnoticed by the human eye of an expert. This ability to identify imperfections that might not be obvious to a human observer underlines the usefulness and potential improvement in the accuracy of the detection process. The technology provides a more detailed and objective view of the items under study, which can lead to a more thorough assessment of the quality of products or materials. The algorithm's ability to highlight defects that may have been previously overlooked by experts offers valuable insight into quality control and opens up new opportunities for more rigorous analysis in various industrial applications. The automated approach is designed to enhance efficiency, reduce errors, and provide a more objective assessment, offering distinct advantages when compared to the manual methods based on CENEX.

4. Conclusions

The findings of this study reveal that the application of an image processing-based approach for the segmentation and measurement of pores in low-quality industrial radiographic images has proven to be highly accurate and reliable. This is evidenced by the comparison of the defect areas calculated by the proposed algorithm with those provided by experts. The errors in the measurements are less than 0.1 mm², demonstrating the consistency and accuracy of the method. Furthermore, the number of detected contours matches the number of defects identified by experts, supporting the effectiveness of the approach in pore detection. With a precision of 97.52%, a recall of 98.33%, and an F1-Score of 97.92%, the method demonstrates its versatility in accurately identifying and measuring pores in low-quality images, making it a valuable tool for a broader range of applications.

However, it is relevant to note that the algorithm has some limitations, detecting three false positives and two false negatives. Despite notable achievements in accuracy, recall and F1-Score, these results indicate instances in which the method incorrectly identified pores that were not defects (false positives) and failed to detect some real defects (false negatives). As a result of this investigation, future work aimed at addressing the identified shortcomings could involve refining the image processing-based approach for pore segmentation and measurement. Potential avenues for improvement may include the exploration of alternative filtering methods to optimize contrast and illumination in X-ray images. The imperative to study other filtering methods for enhancing contrast and illumination emphasizes the ongoing need for research to enhance accuracy and address potential sources of error within the methodology. This iterative refinement process is crucial for consistently advancing the reliability and precision of the method, ensuring its effectiveness across various industrial applications.

This approach offers a valuable tool for industrial radiography specialists, with high potential for inspection and quality control applications. The results obtained indicate that the analysis approach employed is reliable and capable of accurately estimating defect areas in X-ray images. It serves as a valuable asset for industries necessitating meticulous inspection and maintenance, thus contributing to the overall reliability and functionality of agricultural equipment.

5. References

Açar, I., Çevik, B., & Gülenç, B. (2023). Weldability of dissimilar stainless steels by MIG welding with different gas combinations. *Sādhanā*, *48*(2), 69.

Aslam, Y., Santhi, N., Ramasamy, N., & Ramar, K. (2019). A modified adaptive thresholding method using cuckoo search algorithm for detecting surface defects. *International Journal of Advanced Computer Science and Applications*, *10*(5), 214-220.

Batallas, A. L., Paucar, J. B., Quevedo, J. P., & Ordoñez, H. T. (2020). Una revisión de las métricas aplicadas en el procesamiento de imágenes. *RECIMUNDO: Revista Científica de la Investigación y el Conocimiento*, *4*(3), 267-273.

BD, R. V. (2020). Deep Learning for Quality Prediction in Dissimilar Spot Welding DP600-AISI304, Using a Convolutional Neural Network and Infrared Image Processing. European Modeling & Simulation Symposium,

Choi, K.-H., & Ha, J.-E. (2023). An adaptive threshold for the canny edge with actor-critic algorithm. *IEEE Access*.

Contreras, C. E., Soldara, S. M. M., Cruz, O. S., Garcia, S. B., & Zarate, J. D. (2022). SISTEMA DE VISIÓN DE DIMENSIONAMIENTO MORFOLÓGICO PARA LA COLOCACIÓN DE FRENOS CORRECTORES DENTALES (MORPHOLOGICAL SIZING VISION SYSTEM FOR THE PLACEMENT OF DENTAL CORRECTIVE BRACES). *Pistas Educativas*, *43*(141).

Duan, F., Yin, S., Song, P., Zhang, W., Zhu, C., & Yokoi, H. (2019). Automatic welding defect detection of x-ray images by using cascade adaboost with penalty term. *IEEE Access*, *7*, 125929-125938. https://doi.org/https://10.1109/ACCESS.2019.2927258

Dwivedi, S. K., Vishwakarma, M., & Soni, A. (2018). Advances and researches on non destructive testing: A review. *Materials Today: Proceedings*, *5*(2), 3690-3698. https://doi.org/https://doi.org/10.1016/j.matpr.2017.11.620

Eckel, S., Zscherpel, U., Huthwaite, P., Paul, N., & Schumm, A. (2020). Radiographic film system classification and noise characterisation by a camera-based digitisation procedure. *NDT & E International*, *111*, 102241. https://doi.org/https://doi.org/10.1016/j.ndteint.2020.102241

Golodov, V., & Maltseva, A. (2022). Approach to weld segmentation and defect classification in radiographic images of pipe welds. *NDT & E International*, *127*, 102597. https://doi.org/https://doi.org/10.1016/j.ndteint.2021.102597

Gong, Y., Luo, J., Shao, H., & Li, Z. (2022). A transfer learning object detection model for defects detection in X-ray images of spacecraft composite structures. *Composite Structures*, *284*, 115136. https://doi.org/https://doi.org/10.1016/j.compstruct.2021.115136

Haievskyi, O., Kvasnytskyi, V., Haievskyi, V., & Zvorykin, C. (2020). Analysis of the influence of the systemic welding coordination on the quality level of joints. *Восточно-Европейский журнал передовых технологий*, *5*(1-107), 98-109.

Hernández, A. E., Villarinho, L. O., Ferraresi, V. A., Orozco, M. S., Roca, A. S., & Fals, H. C. (2020). Optimization of resistance spot welding process parameters of dissimilar DP600/AISI304 joints using the infrared thermal image processing. *The International Journal of Advanced Manufacturing Technology*, *108*, 211-221. https://doi.org/https://doi.org/10.1007/s00170-020-05374-y

Hu, A., Wu, L., Huang, J., Fan, D., & Xu, Z. (2022). Recognition of weld defects from X-ray images based on improved convolutional neural network. *Multimedia Tools and Applications*, *81*(11), 15085-15102. https://doi.org/https://doi.org/10.1007/s11042-022-12546-3

Jonsson, B., Dobmann, G., Hobbacher, A., Kassner, M., & Marquis, G. (2016). *IIW guidelines on weld quality in relationship to fatigue strength* (Vol. 158). Springer. https://doi.org/https://doi.org/10.1007/978-3-319-19198-0

Kappaun, R., Jabuonski Jr, R. J., Vetturazzi, R., & de Meira Jr, A. D. (2021). NUMERICAL FATIGUE EVALUATION IN AGRICULTURAL EQUIPMENT WELDED UNIONS.

Kumar, A., & Sodhi, S. S. (2020). Comparative analysis of gaussian filter, median filter and denoise autoenocoder. 2020 7th International Conference on Computing for Sustainable Global Development (INDIACom),

León Ovelar, L. R., Cikel, K., & Gregor Recalde, D. O. (2021). Inteligencia artificial al servicio de la salud pública: caso de estudio detección temprana de focos larvarios de mosquitos. *XXXVII Congreso Interamericano Virtual de Ingeniería Sanitaria y Ambiental*,

Li, L., Ren, J., Wang, P., Gao, H., Sun, M., Sha, B., . . . Li, X. (2023). A pixel-level weak supervision segmentation method for typical defect images in X-ray inspection of solid rocket motors combustion chamber. *Measurement*, *211*, 112497. https://doi.org/https://doi.org/10.1016/j.measurement.2023.112497

Li, L., Ren, J., Wang, P., Lü, Z., Li, X., & Sun, M. (2022). An adaptive false-color enhancement algorithm for super-8-bit high grayscale X-ray defect image of solid rocket engine shell. *Mechanical Systems and Signal Processing*, *179*, 109398. https://doi.org/https://doi.org/10.1016/j.ymssp.2022.109398

Liang, H., Li, N., & Zhao, S. (2021). Salt and pepper noise removal method based on a detail-aware filter. *Symmetry*, *13*(3), 515.

Liu, B., & Yang, T. (2017). Image analysis for detection of bugholes on concrete surface. *Construction and Building Materials*, *137*, 432-440. https://doi.org/https://doi.org/10.1016/j.conbuildmat.2017.01.098

Liu, W., Shan, S., Chen, H., Wang, R., Sun, J., & Zhou, Z. (2022). X-ray weld defect detection based on AF-RCNN. *Welding in the World*, *66*(6), 1165-1177. https://doi.org/https://doi.org/10.1007/s40194-022-01281-w

McPheron, T. J., & Stwalley, R. M. (2022). Engineering Challenges Associated with Welding Field Repairs. In *Engineering Principles-Welding and Residual Stresses*. IntechOpen.

Melibaev, M., Negmatullaev, S., Farkhodkhon, N., & Behzod, A. (2022). TECHNOLOGY OF REPAIR OF PARTS OF AGRICULTURAL MACHINES, EQUIPMENT WITH COMPOSITE MATERIALS. Conference Zone,

Niño, C., Castro Casadiego, S., Medina Delgado, B., Camargo, L., & Guevara-Ibarra, D. (2021). Comparativa entre la técnica de umbralización binaria y el método de Otsu para la detección de personas. *Revista UIS ingenierías*, *20*(2 (2021)), 65-74. https://doi.org/https://10.18273/revuin.v20n2-2021006

Patil, R. V., Reddy, Y., & Thote, A. M. (2021). Multi-class weld defect detection and classification by support vector machine and artificial neural network. Modeling, Simulation and Optimization: Proceedings of CoMSO 2020,

Pérez de la Parte, M., Espinel Hernández, A., Sánchez Orozco, M. C., Sánchez Roca, A., Jimenez Macias, E., Blanco Fernández, J., & Carvajal Fals, H. (2022). Effect of zinc coating on delay nugget formation in dissimilar DP600-AISI304 welded joints obtained by the resistance spot welding process. *The International Journal of Advanced Manufacturing Technology*, *120*(3-4), 1877-1887. https://doi.org/https://doi.org/10.1007/s00170-022-08849-2

Radi, D., Abo-Elsoud, M. E. A., & Khalifa, F. (2022). Accurate segmentation of weld defects with horizontal shapes. *NDT & E International*, *126*, 102599. https://doi.org/https://doi.org/10.1016/j.ndteint.2021.102599

Rafiei, M., Raitoharju, J., & Iosifidis, A. (2023). Computer vision on x-ray data in industrial production and security applications: A comprehensive survey. *Ieee Access*, *11*, 2445-2477.

Ríos, L., Roncaglia, G., & Ortiz de Zárate, R. (2022). Análisis y clasificación de ladrillos de hormigón celular a través de imágenes.

Szusta, J., Derpeński, Ł., Karakaş, Ö., Tüzün, N., & Dobrzański, S. (2023). Effect of Welding Process Parameters on the Strength of Dissimilar Joints of S355 and Strenx 700 Steels Used in the Manufacture of Agricultural Machinery. *Materials*, *16*(21), 6963.

Truong, M. T. N., & Kim, S. (2018). Automatic image thresholding using Otsu's method and entropy weighting scheme for surface defect detection. *Soft Computing*, *22*, 4197-4203. https://doi.org/https://doi.org/10.1007/s00500-017-2709-1

Tyystjärvi, T., Virkkunen, I., Fridolf, P., Rosell, A., & Barsoum, Z. (2022). Automated defect detection in digital radiography of aerospace welds using deep learning. *Welding in the World*, *66*(4), 643-671. https://doi.org/https://doi.org/10.1007/s40194-022-01257-w

Wang, D., & Gao, W. (2021). Study of x-ray image defect detection methods for girth welds. Second IYSF Academic Symposium on Artificial Intelligence and Computer Engineering,

Wang, S., Xia, X., Ye, L., & Yang, B. (2021). Automatic detection and classification of steel surface defect using deep convolutional neural networks. *Metals*, *11*(3), 388. https://doi.org/https://doi.org/10.3390/met11030388

Wang, X., & Yu, X. (2023). Understanding the effect of transfer learning on the automatic welding defect detection. *NDT & E International*, *134*, 102784. https://doi.org/https://doi.org/10.1016/j.ndteint.2022.102784

Wang, Z., Lei, X., & Gao, W. (2022). Study on SDR extraction of ring weld defects of pipeline. *Welding in the World*, *66*(8), 1645-1652. https://doi.org/https://doi.org/10.1007/s40194-022-01323-3

Wells, T., & Miller, G. (2022). Students' Perspectives on Using Virtual Reality Technology in a University-level Agricultural Mechanics Course. *Journal of Agricultural Education*, *63*(2).

Yahaghi, E., Mirzapour, M., & Movafeghi, A. (2021). Comparison of traditional and adaptive multi-scale products thresholding for enhancing the radiographs of welded object. *The European Physical Journal Plus*, *136*, 1-13.

Zhan, X., Zhang, D., Yu, H., Chen, J., Li, H., & Wei, Y. (2018). Research on X-ray image processing technology for laser welded joints of aluminum alloy. *The International Journal of Advanced Manufacturing Technology*, *99*, 683-694. https://doi.org/https://doi.org/10.1140/epjp/s13360-021-01733-0

Zhang, B., Wang, X., Cui, J., Wu, J., Wang, X., Li, Y., . . . Wu, W. (2023). Welding defects classification by weakly supervised semantic segmentation. *NDT & E International*, 102899. https://doi.org/https://doi.org/10.1016/j.ndteint.2023.102899

Zhang, J., Guo, Z., Jiao, T., & Wang, M. (2018). Defect detection of aluminum alloy wheels in radiography images using adaptive threshold and morphological reconstruction. *Applied Sciences*, *8*(12), 2365. https://doi.org/https://doi.org/10.3390/app8122365

6. Additional Information

6.1 Conflicts of Interest